Geophysical Journal International

Geophys. J. Int. (2020) **220,** 2039–2055
Advance Access publication 2019 December 16
GJI Geodynamics and tectonics

doi: 10.1093/gji/ggz564

Geodetic evidence for shallow creep along the Quito fault, Ecuador

J. Mariniere [1], J.-M. Nocquet [2,3] C. Beauval,[1] J. Champenois,[4] L. Audin,[1] A. Alvarado,[5] S. Baize[4] and A. Socquet[1]

[1]*Université Grenoble Alpes, Université Savoie Mont Blanc, CNRS, IRD, IFSTTAR, ISTerre,* 38000 *Grenoble France.*
E-mail: judith.mariniere@univ-grenoble-alpes.fr
[2]*Université Côte d'Azur, IRD, CNRS, Observatoire de la Côte d'Azur, Géoazur,* 06560 *Valbonne, France*
[3]*Institut de Physique du Globe de Paris, Sorbonne Paris Cité, CNRS, Paris, France*
[4]*Institut de Radioprotection et Sûrete´ Nucle´aire BP*17, 92262 *Fontenay-aux-Roses, France*
[5]*Escuela Polite´cnica Nacional Instituto Geofi´sico, Ladro´n de Guevara E*11-253 *Apartado* 2759 *Quito, Ecuador*

Accepted 2019 December 6. Received 2019 November 10; in original form 2019 April 4

SUMMARY

Quito, the capital city of Ecuador hosting ∼2 million inhabitants, lies on the hanging wall of a ∼60-km-long reverse fault offsetting the Inter-Andean Valley in the northern Andes. Such an active fault poses a significant risk, enhanced by the high density of population and overall poor building construction quality. Here, we constrain the present-day strain accumulation associated with the Quito fault with new Global Positioning System (GPS) data and Persistent Scatterer Interferometric Synthetic Aperture Radar (PS-InSAR) analysis. Far field GPS data indicate 3–5 mm yr^{-1} of horizontal shortening accommodated across the fault system. In the central segment of the fault, both GPS and PS-InSAR results highlight a sharp velocity gradient, which attests for creep taking place along the shallowest portion of the fault. Smoother velocity gradients observed along the other segments indicate that the amount of shallow creep decreases north and south of the central segment. 2-D elastic models using GPS horizontal velocity indicate very shallow (<1 km) locking depth for the central segment, increasing to a few kilometres south and north of it. Including InSAR results in the inversion requires locking to vary both along dip and along strike. 3-D spatially variable locking models show that shallow creep occurs along the central 20-km-long segment. North and south of the central segment, the interseismic coupling is less resolved, and data still allows significant slip deficit to accumulate. Using the interseismic moment deficit buildup resulting from our inversions and the seismicity rate, we estimate recurrence time for magnitude 6.5 + earthquake to be between 200 and 1200 yr. Finally, PS-InSAR time-series identify a 2 cm transient deformation that occurred on a secondary thrust, east of the main Quito fault between 1995 and 1997.

Key words: Creep and deformation; Radar interferometry; Satellite geodesy; South America; Continental tectonics: compressional; Dynamics and mechanics of faulting.

1 INTRODUCTION

Subduction zones not only produce the largest earthquakes on Earth through seismic slip at the megathrust, but also induce long-term strain within the overriding plate, accommodated by earthquakes occurring on crustal faults. Although of lower magnitude than the largest subduction earthquakes, crustal earthquakes rupturing at shallow depths pose a significant hazard often directly threatening highly populated areas.

Along the Nazca/South America subduction zone, the Ecuadorian Andes is among the areas where crustal earthquakes have been particularly damaging. For instance, in 1797, one of the largest crustal earthquakes ever documented in South America (*M* 7.6–7.9, Beauval *et al.* 2010) led to a complete destruction of the city of Riobamba in central Ecuador (Fig. 1a). In 1949, a M_w 6.8 earthquake occurred in the Inter-Andean Valley near Ambato, generating numerous landslides and killing more than 5000 people (e.g. https://earthquake.usgs.gov/learn/today/index.php?month=8&day=5, Fig. 1a).

Both the 1797 and 1949 earthquakes occurred along the Chingual–Cosanga–Pallatanga–Puna fault system (hereafter referred to as the CCPP) delimiting the eastern boundary of the North Andean Sliver, a continental domain moving northeastward at 8–10 mm yr^{-1} with respect to the stable part of the South America Plate (Pennington 1981; Nocquet *et al.* 2014; Alvarado *et al.* 2016; Yepes *et al.* 2016; Mora-Paez *et al.* 2019). Although crustal faults bounding the North Andean Sliver show the fastest slip rates in Ecuador (Dumont *et al.* 2006; Tibaldi *et al.* 2007; Nocquet *et al.* 2014; Baize *et al.* 2015; Alvarado *et al.* 2016), large historical

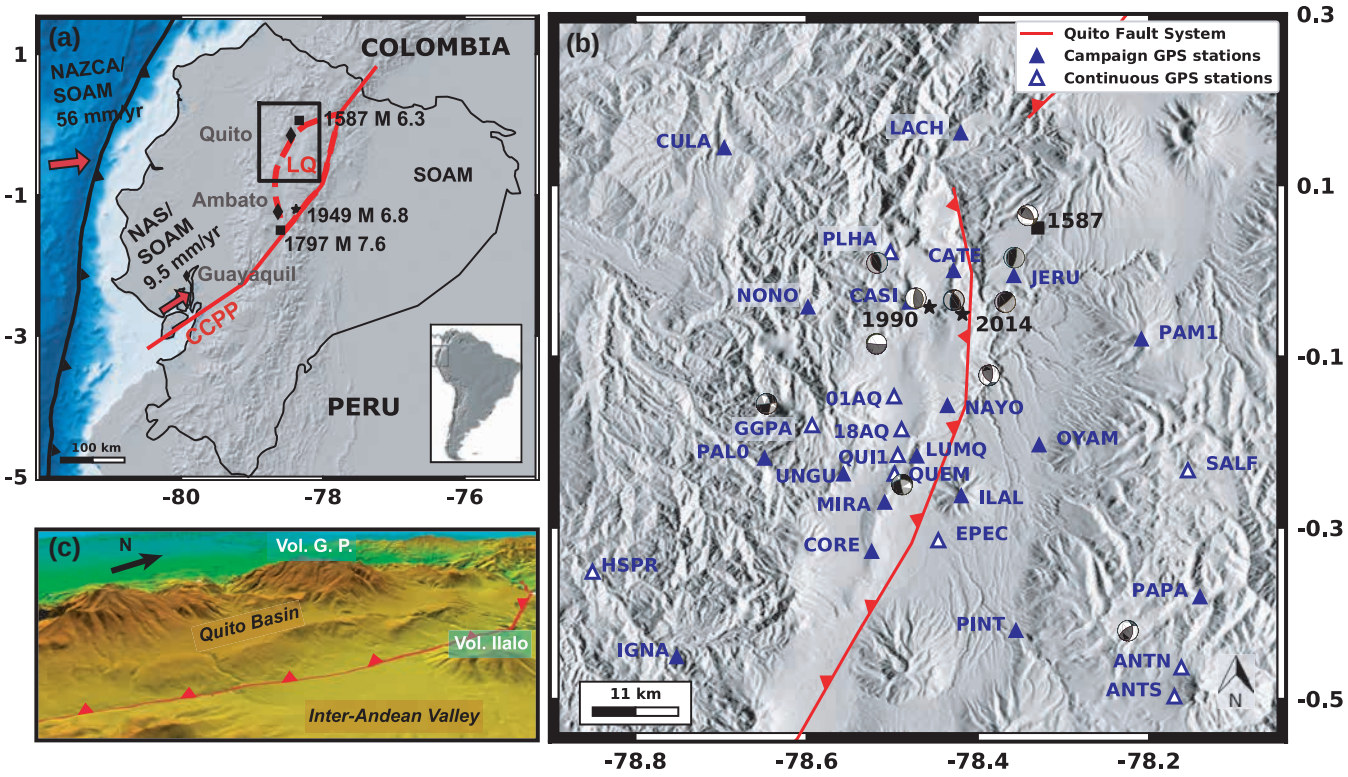

Figure 1. (a) Ecuador geodynamic and seismotectonic settings**.** The continuous red line indicates the CCPP (Chingual-Cosanga-Pallatanga-Puna´) fault system (after Alvarado *et al.* 2016), delimiting the eastern boundary of the North Andean Sliver (NAS). LQ is the Latacunga-Quito block proposed in Alvarado *et al.* (2014) with its western boundary indicated by the dashed red line. Black squares and stars are historical and instrumental earthquakes, respectively. The black line with triangles indicates the location of the trench. The black rectangle indicates the area shown in (b). (b) Seismotectonic map of the Quito region. Blue triangles are campaign GPS stations and white triangles are continuous GPS stations. The simplified surface trace of the Quito reverse Fault System is shown by the barbed red line. Focal mechanism solutions of earthquakes above magnitude 4, during the 1990–2011 period, are from Alvarado *et al.* (2014). GPS PLHA is located on the top of the Pululahua Volcano, GPS GGPA is on top of the Guagua Pichincha and ILAL is on the top of the Ilalo. Square: 1587 *M*6.3 historical earthquake (location from Beauval *et al.* 2010), stars: 1990 M_w equivalent 5.3 Pomasqui and 2014 M_w 5.1 earthquakes. (c) 3-D view of Quito in the Inter-Andean Depression. Los Chillos Valley is the Inter-Andean Valley represented east of the QFS. In white letters are the volcanoes cited in the text. Vol G. P.: Volcano Guagua Pichincha.

earthquakes (Beauval *et al.* 2010, 2013), seismologically recorded moderate size earthquakes (Vaca *et al.* 2019) and geomorphic markers of neotectonics faulting (Alvarado *et al.* 2016) witness active deformation distributed within the North Andean Sliver. In central Ecuador, Alvarado *et al.* (2016) proposed the existence of an additional Latacunga-Quito block encompassing the Inter-Andean valley and the eastern cordillera from latitude 1.5°S to the strike-slip Guayllabamba fault (lat. 0°), connecting the Quito fault system north of Quito to the CCPP (Fig. 1a).

Here, we focus on the 60-km-long north–south striking Quito fault, that delimits the western boundary of the Latacunga-Quito block, where ∼2 million people are living in the capital city of Ecuador and its surroundings. In that area, the 20-km-wide Inter-Andean depression separating the western and eastern Andean cordillera is offset by a series of *en echelon* thrusts separating the lower Los Chillos Valley from the higher Quito Basin, with an average cumulated uplift of 400 m (Fig. 1c). Fault related folds in quaternary volcanoclastic deposits, hanging palaeo-valleys and records of disrupted drainage patterns confirm the recent activity of the Quito thrust fault (Alvarado *et al.* 2014).

Since the development of the Ecuadorian seismic network in the early 1990s, seven earthquakes of magnitude (m_b) above 4.0 have been recorded in the Quito area. Among them, the Pomasqui earthquake (M_w 5.3, 10 August 1990) killed three people, damaged about 900 buildings and houses and triggered many landslides along the panamerican road (https://www.igepn.edu.ec/servicios/noticias/466-sismo-de-pomasqu%C3%AD-10-de-agosto-de-1990). More recently, the 12 August 2014 (M_w 5.1) earthquake killed four people, and triggered landslides north of Quito. The historical records spanning almost five centuries, show that the city experienced MSK (Medvedev-Sponheuer-Karnik) intensities in the ranges VII–VIII at least five times (Pino & Yepes 1990; Egred 2009). Using the historical intensity records, Beauval *et al.* (2010) estimated a 6.3–6.5 magnitude for an event in 1587 at a location near Guayllabamba in the northern part of the Quito fault system (Fig. 1b). The most damaging earthquake recorded for Quito occurred in 1859 (Intensity VII–VIII), but whether it occurred on a crustal fault remains unclear (Beauval *et al.* 2010). Focal mechanisms show predominantly reverse mechanisms (Guillier *et al.* 2001; Alvarado *et al.* 2014; Vaca *et al.* 2019) in agreement with a dominant east–west shortening across the Quito fault. Secondary thrusts and strike slip faults are documented east of the main fault in the Los Chillos Valley and regularly host small earthquakes (Alvarado *et al.* 2014).

Preliminary GPS results along a profile in central Quito showed 4 mm yr^{-1} of shortening across the fault. Using simple 2-D elastic screw dislocation models, Alvarado *et al.* (2014) suggest a shallow locking depth of 3 km. In this study, we use an augmented GPS velocity field and spatially dense InSAR data to precisely

quantify the kinematics in the Quito area and to evaluate the current rate of slip deficit accumulation along the different segments of the fault. We first derived optimal values for the fault geometry and its slip deficit using a 2-D Bayesian inversion. Finally, the results of the 2-D modelling are used as input parameters to constrain a spatially variable interseismic coupling model of the fault.

2 DATA SET

2.1 GPS data

We use a combination of 18 campaign mode GPS sites with 11 continuous GPS in the area of Quito (Fig. 1b, Table 1). Campaign sites have a minimum observation span of 8 yr (except LACH, 3.5 years) and of 3.2 yr for continuous GPS. All data used in this study were collected before the 2016 M_w 7.8 Pedernales earthquake that induced coseismic offsets of a few centimetres (Nocquet *et al.* 2016; Mothes *et al.* 2018) and centimetres level post-seismic deformation (Rolandone *et al.* 2018) in the Quito area. The GPS dataset spatially samples the whole Quito area with a higher density in its central part.

We process the 24-hr-long session data using the GAMIT/GLOBK 10.70 software (Herring *et al.* 2018) to obtain daily loosely constrained solutions. We derive the time-series by expressing the loosely constrained solutions in the ITRF2014 (Altamimi *et al.* 2016) with a 7-parameter transformation using regional IGS sites (http://www.igs.org). For the continuous GPS data, we first evaluate the time correlated noise for a model including white and flicker noise using the Maximum Likelihood Estimation algorithm embedded in the CATS software (Williams 2005). We then convert the flicker noise parameters obtained from the CATS analysis to equivalent random noise parameters that can then be used in the GLOBK Kalman filter (Floyd *et al.* 2010). For the campaign data, we apply noise parameters corresponding to the median value obtained from the continuous GPS analysis. The final velocity solution is obtained running the GLOBK Kalman filter. Such an approach provides conservative estimates of velocity uncertainties. Campaign mode sites with $\sim$15 yr of measurements and 3 campaign show velocity uncertainties between 0.15 and 0.35 mm yr^{-1} at the 1σ confidence level and continuous GPS sites with 3–8 yr of data have uncertainties between 0.2 and 0.6 mm yr^{-1} depending on the length and noise properties of the time-series. For subsequent modelling, we express our velocity field in a reference frame corresponding to the non-deforming part of the fault footwall (Fig. 2). This is achieved by estimating a rigid body motion using the velocities from a subset of GPS sites (ANTN, ANTS, OYAM, PAM1, PAPA and PINT) showing negligible internal deformation (weighted root-mean-square of 0.26 mm yr^{-1}). We also estimated the vertical rates for three continuous GPS stations close to the Quito fault: QUEM (2007.9–2016.3), QUI1 (2000.0–2010.3) and EPEC (2013.0–2016.3). In the ITRF2014, their vertical velocity estimates are QUEM: -1.4 ± 0.8, QUI1: -0.8 ± 0.8, EPEC -0.6 ± 1.0, all values in mm yr^{-1} and positive upwards with their associated uncertainty provided at the 95 per cent confidence level. These values indicate a relative vertical subsidence of GPS sites located on the hanging wall with respect to the footwall, but uncertainties leave also the possibility of opposite motion. Alternatively, we estimate the relative velocity of QUEM with respect to EPEC using the baseline time-series (QUI1 and EPEC do not have a common observation period, see Fig. S5). We now find an uplift rate of QUEM with respect to EPEC of 0.4 ± 1.0 mm yr^{-1}. Because of these contradictory results, we chose not to use the vertical rates in the subsequent modelling.

2.2 InSAR data

Additionally, we use InSAR results from 19 European Remote Sensing (ERS) acquisitions collected in descending mode between May 1993 and September 2000 to determine mean line-of-sight (LOS) velocity in the Quito area (Champenois *et al.* 2013, 2015). Quito and its surroundings include vegetated, cultivated and rapidly changing urban areas, involving a rapid loss of coherence of the radar phase with time. We therefore use the Persistent Scatterer technique (PS-InSAR) implemented in the Stanford Method for Persistent Scatterer version 4.0 (StaMPS) software package (Hooper 2008). The StaMPS PS-InSAR approach identifies individual radar-bright and phase-stable points and allows to follow their change of phase over long periods without the assumption of linear displacement. The radar images are coregistered to the same master image, here 06 May 1998, selected in the middle of the observation period. As a result, the analysis provides 18 values of LOS change for every PS pixel during the 1993–2000 period. Interferograms are corrected for changes in atmospheric delay during the PS processing using space and time filters described in Hooper *et al.* (2007). The resulting mean LOS rate map is shown in Fig. 3(a). Aside the mean LOS rate, the StaMPS approach provides formal errors of the mean velocity and the LOS displacement time-series at each acquisition date (Fig. 3c). We carefully check the time-series and find that for pixels located southwest of the Ilalo Volcano, LOS displacements during the 1995–1996 period exhibit significant departure from a constant velocity (Figs 3d–h). Additional information about this transient motion is provided in the discussion paragraph. In order to correct for this localized transient signal, we use the following approach: for every pixel, we extract the full time-series and solve for a trend plus an offset at 1995.5 using weighted least-squares. If the estimated offset is larger than two times its formal uncertainty, the retained LOS velocity is the one obtained by simultaneously estimating a slope and an offset using least-squares. If the offset is less than twice its formal uncertainty, the retained LOS velocity is the one using all dates of the time-series without an offset correction (Fig. 3f). Finally, we keep only pixels with a formal error lower than 0.9 mm yr^{-1} for subsequent modelling. Such a value is found to ensure kilometres' scale consistency of LOS rates. Indeed, using a larger threshold value provides highly spatially scattered LOS rates, especially in the high relief of the western Cordillera (Figs 1c and 3b). With a total of more than 68 000 PS, the final LOS rate map is almost continuous over a length of 30 km along the Quito Fault system. Although the inconsistency of GPS vertical rates prevents a full comparison of InSAR and GPS results to be made, we compare the relative 3-D vector of GPS site QUEM with respect to EPEC projected along the LOS and PS-InSAR results. We find a differential GPS LOS rate of 1.63 mm yr^{-1} to be compared to 1.49 mm yr^{-1} for the PS-InSAR results, suggesting a good consistency between the GPS and PS-InSAR results.

2.3 Correction of the elastic contribution from the subduction interseismic loading

Locking along the subduction interface induces shortening in the east–west direction, a signal that adds up to the signature of east–west shortening induced by the Quito fault. We use the interseismic

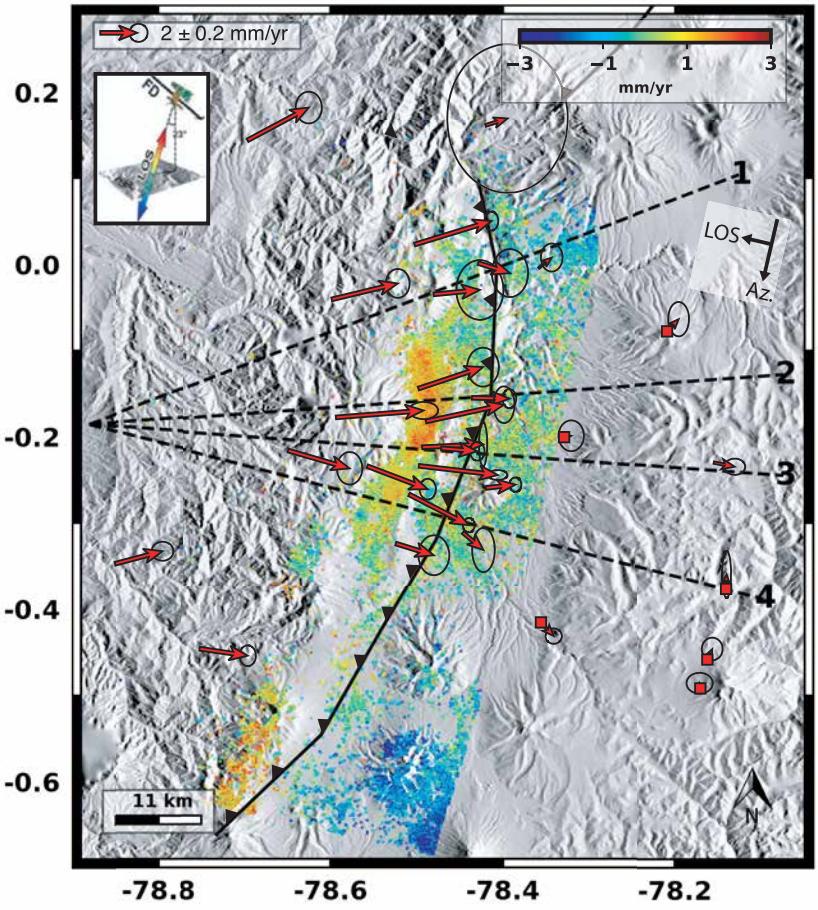

Figure 2. Horizontal GPS velocity field (1994–2016) and PS-InSAR LOS velocity map derived from 19 ERS acquisitions collected in descending mode between May 1993 and September 2000. Positive displacement corresponds to motion towards the satellite. The values are in mm yr^{-1} and colour-coded according to the scale shown on the top right. Arrows are the GPS horizontal velocity field with respect to a reference frame defined by minimizing the velocities of GPS sites ANTN, ANTS, OYAM, PAM1, PAPA and PINT. Error ellipses are 95 per cent confidence level. The barbed black line shows the simplified surface trace of the Quito thrust fault. Dashed lines indicate the location of the four profiles used for the 2-D modelling.

model from Nocquet *et al.* (2016) to predict the contribution of elastic deformation induced by the subduction and remove it from our geodetic data in the Quito area. Expressed in an overriding plate reference frame (here, the North Andean Sliver), the elastic contribution due to locking along the megathrust is 2.5 mm yr^{-1} for the westernmost site of our networks and 1.3 mm yr^{-1} for the easternmost one, for the horizontal components. With respect to our stable hanging wall fault reference frame (see Section 2.2), this translates into an almost linear east–west shortening rate of 0.013 mm yr^{-1} per km. Although small compared to the gradient observed across the Quito fault, applying this correction reduces by 0.8 mm yr^{-1} the relative horizontal shortening over our GPS network. For the vertical component, the maximum prediction reaches at most 0.2 mm yr^{-1} and is therefore negligible. Both the GPS horizontal velocity and the InSAR LOS rates were corrected prior modelling.

3 RESULTS

The horizontal GPS velocity field shows a general pattern of 3–4.5 mm yr^{-1} of EW shortening between sites located west of the Quito fault system and sites located in the eastern part of the Inter-Andean valley (Fig. 2). Unlike most across fault profiles which show a gentle monotonic decrease of velocity magnitude, here we note that velocities on the hanging wall, in the Quito city area, show a velocity equal to or larger than the far-field velocity (QUEM 4.3 mm yr^{-1} and 18AQ 4.3 mm yr^{-1} compared to PAL0 and UNGU 3.5 mm yr^{-1}). Such a pattern is a potential indication of slip on the fault at shallow depth. Furthermore, the gradient across the Quito fault appears to be sharp: the velocity magnitude decreases by 50 per cent over a distance of 2 km (e.g. QUI1-LUMQ) and becomes negligible 10 km away from the fault (OYAM 0.4 mm yr^{-1}, Fig. 2). This pattern is an additional direct evidence of a very shallow locking depth.

PS-InSAR results also show a general LOS rate gradient of ∼2 mm yr^{-1} between the hanging wall and the footwall of the Quito fault. Maximum LOS rates are found in the central Quito area, with a sharp LOS rate decrease from 2 to 0 mm yr^{-1} over a distance of 2 km (Fig. 2). Such a gradient indicates either a decrease of east velocity, a decreasing uplift rate, or a combination of both. The sharp LOS gradient spatially correlates with the high-shortening rate seen in the GPS (e.g. 01AQ/18AQ to NAYO and QUI1 to LUMQ, Fig. 2) and therefore also constitutes an observation independently confirming the existence of shallow creep and an overall very shallow locking depth. In the central western part of the Quito Basin, close to the eastern flank of Guagua Pichincha volcano, the InSAR data show an opposite gradient with LOS rates decreasing westward. We

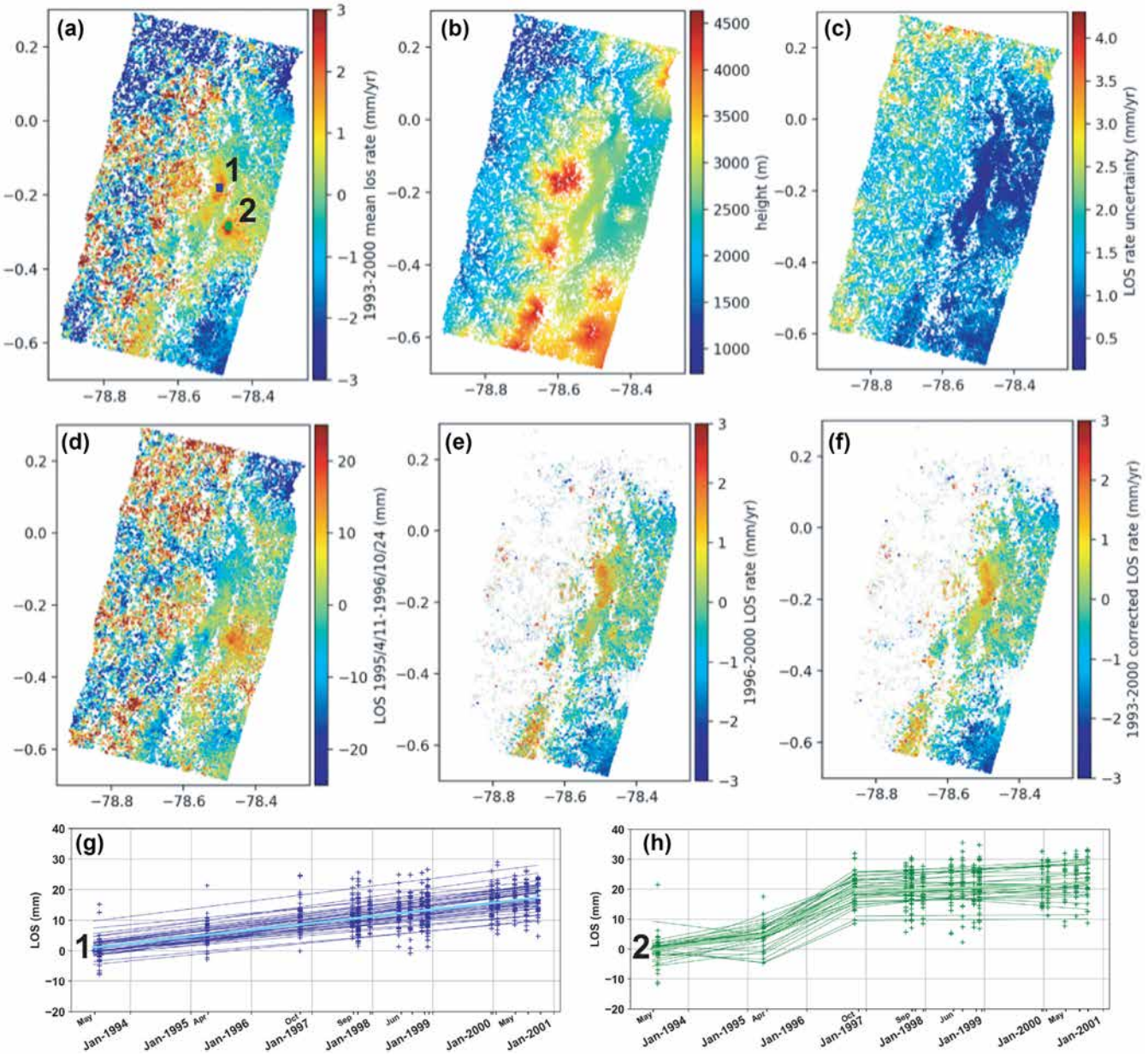

Figure 3. (a) Mean LOS rate map from 19 ERS acquisitions collected in descending mode between 1993/05/23 and 2000/09/27. (b) Topography elevation. (c) LOS rate uncertainty map. d) LOS displacement map between 1995/04/11and 1996/10/23. (e) LOS rate map between 1996/10/23 and 2000/09/27. (f) LOS rate map from 1993/05/23 and 2000/09/27 with the 1995–1996 transient signal removed (see text) (g–h) LOS time-series for SAR pixels located at the areas 1 and 2 indicated in (a). Dark (blue and green) lines are the slope estimated for the time-series for every pixel and the thick light (blue and green) line indicates the median slope of all pixels time-series. For (g) the thick light blue slope is estimated using all the data, while for h) the thick light green slope has been estimated for three different periods: 1993/05/23–1995/04/11; 1995/04/11–1996/10/23 and 1996/10/23–2000/09/27.

further note that the maximum LOS rate is offset by 3 km to the west of the fault trace, possibly indicating creep rates changing with depth.

As secondary features, GPS velocities show some changes of shortening direction, being N70° in the northern part of the fault, N90° in the central part and N110° in its southern part. Roughly, this rotation of shortening direction corresponds to the average rotation of the fault strike, thus implying purely reverse motion across each individual segment. Both north and south of central Quito, the InSAR results show smoother gradient of LOS rates possibly reflecting along strike variations of the amount the shallow creep. Finally, we also note that despite the removal of the transient deformation seen in the PS-InSAR analysis for the 1995–1996 period south west of the Ilalo Volcano, a small (1 mm yr^{-1}) signal persists in that area (location of point 2 in Fig. 3a or Fig. 9c)

4 MODELLING APPROACH

4.1 Potential pichincha volcano contribution to the deformation field

The change of shortening direction observed in the horizontal GPS velocity field raises the question of whether the velocity field or a fraction of it could be related to a volcanic deformation of the

nearby Guagua Pichincha Volcano, located about 15 km west of the Quito fault. A magmatic eruption phase occurred between 1998 and 2001 overlapping the acquisition period for the SAR data used in our study. Garcia-Aristizabal *et al.* (2007) estimated a magma storage between 4 and 11–12 km beneath the Guagua Pichincha caldera. Increase or decrease in pressure at such a depth would certainly not be able to explain the sharp gradient observed near the Quito Fault trace, but could impact our InSAR results with an additional gradient in the Quito area. We therefore carefully check any non-linear behaviour in the PS time-series corresponding to the eruptive period and did not find any significant departure from a constant velocity aside the one already mentioned near the Ilalo Volcano (Fig. 3). More recently, Morales Rivera *et al.* (2016) identified 6.5 cm of localized subsidence from mid-2007 to August 2009 from InSAR data. They modelled the InSAR signal by a single shallow (3 km) pressure source inducing negligible deformation a few kilometres away from the Guagua Pichincha caldera. The time-series of CGPS QUEM starting in December 2007 do not show any departure from the average linear trend for this period (Fig. S5d). Therefore, we believe that the Pichincha volcanic activity has a minor impact on our velocity field and certainly does not impact the main pattern of the velocity field such as the sharp gradient observed across the Quito fault.

4.2 Possible anelastic contribution to surface deformation

Physical models of thrust and fold evolution show that the long-term displacement at the surface results from the combination of slip along the fault at depth and of distributed folding above the fault tip (e.g. Johnson 2018). However, the contribution of anelastic deformation over a few years during the interseismic period is less clear. Although observed high strain near the fault trace has been proposed to include anelastic contribution for the Anza segment of the strike-slip San Jacinto Fault in Southern California (Lindsey *et al.* 2014), we are not aware of similar conclusions for thrust faults. For instance, the narrow strip of high strain rate observed along the Longitudinal Valley Fault in Taiwan, a pattern very like our results for the Quito Fault, is successfully explained using elastic models (Thomas *et al.* 2014). Nonetheless, in the Quito area, the upper stratigraphic layers (several hundreds of metres and even possibly more) are made of intercalated poorly consolidated volcanic ashes and lahar deposits, that certainly reduce the elastic strength and possibly undergo anelastic deformation. Furthermore, very steep slopes along the eastern flanks of the Quito basin (Fig. 1b) are unstable and experience regular landslides, adding to the crustal motion in the PS-InSAR data (GPS sites were chosen away from unstable areas). In the subsequent modelling, we do not account for these processes, but acknowledge that they add some uncertainties, for instance on the amount and location of shallow creep estimates close to the surface.

4.3 Elastic models

Despite the limitations described above, we attempt to quantify the rate of slip deficit accumulation along the Quito fault, assuming that the observed surface displacement can be explained by a set of dislocations at depth in a homogeneous elastic half-space. Although some studies have shown that viscoelastic relaxation plays a critical role for dip-slip faults when modelling the surface velocity during the earthquake cycle (e.g. Segall 2010), purely elastic models are therefore correct to the first order when the observation is made at a date being several times the relaxation time since the last large earthquake, as it is the case for the Quito fault. For instance, Fukahata & Matsu'ura (2006) show that the elastic solution is equivalent to the fully relaxed deformation of a stratified viscoelastic models with a null rigidity of the underlying medium. Elastic models are further useful approximation to estimate the rate of slip deficit accumulation along faults.

Under the elastic assumption, different approaches can be used. A first type of model is to use a semi-infinite edge dislocation ending at a given depth from the surface. Above this depth, the fault is locked. A second approach is to consider the back-slip model (Savage 1983; McCaffrey 2005), where the surface deformation is the sum of the long-term deformation modelled by rigid block motion and a virtual back-slip component aiming at reproducing the effect of a locked fault on the surface velocity field. The back-slip approach (hereafter noted BS) is strictly equivalent to the semi-infinite dislocation model, but offers the advantage of an easier modelling of far-field data by including block rotation for large areas (McCaffrey 2005; Meade & Hager 2005). A third approach is to model the relative motion of tectonic blocks by a flat décollement (hereafter noted FD). Such a flat décollement predicts block-like motion in the far-field of the fault, a progressive decrease of the horizontal velocity spread over distance, centred at the tip of the décollement. In a fourth approach, the décollement merges a ramp slipping from the depth of the décollement to a given depth (hereafter referred as FDR, e.g. Thompson *et al.* 2015; Daout *et al.* 2016a; Daout *et al.* 2016b). In some cases, the flat décollement and ramp corresponds to a real discontinuity imaged from geophysics as it is for the sub-andean domain, east of the Andean cordillera (e.g. Baby *et al.* 2013). But, regardless its actual existence, the slip along a flat décollement offers a convenient way to mimic the block like behaviour in the far field of the fault and the elastic strain perturbation close to the fault. As Daout *et al.* (2016a) write, the FDR has to be considered as a conceptual model simultaneously describing 'both elastic and permanent parts of the surface displacement field at the present time'.

For the BS models, under the assumption that the observed surface velocities do not reflect transient slip, the kinematic consistency and the assumption of constant horizontal slip vector require the long-term slip rate on the ramp to be equal to V_h/cos(dip), where V_h is the horizontal shortening velocity between the two blocks separated by the fault. For the FDR model, one view is that the long-term slip rate on the ramp should also be equal to V_h/cos(dip) to ensure that the fault accommodates all the far field shortening rate. The alternative view is that the slip rate along the flat décollement is transferred to the ramp. In that latter case, the long-term slip rate on the ramp is equal to the shortening rate V_h. In the supplementary material, we show that using one or the other assumption has a marginal impact on our results and all models presented hereafter are for a long-term slip rate equal to V_h/cos(dip).

In the following, we present a step-by-step modelling approach and progressively introduce more complexity as it is required by the data. We start with synthetic 2-D models for the BS, FD and FDR models to discuss the main patterns of the predicted surface velocity and the ability of each of these models to explain our GPS and PS-InSAR observations. Then, we perform a Bayesian exploration of the BS and FD model parameters using only the GPS observation. We discuss the resolution of the searched parameters and show that fitting PS-InSAR data requires introducing a ramp that connect to the flat décollement (FDR model). We then consider a 2-D FDR model including both GPS and PS-InSAR data, that indicates that variable slip along the ramp can simultaneously fit both GPS and

PS-InSAR data. Building upon this result, we present a spatially variable slip 3-D interseismic model that allows us (1) to discuss the along strike and along dip variations of aseismic slip and (2) to quantify the rate of slip deficit accumulation along the whole fault system.

4.4 2-D synthetic elastic models

As a preliminary step before data inversion, we make simple forward models to assess the ability of the different approaches to explain the main patterns present in our GPS and InSAR observations. Figs 4(a)–(d) show the horizontal and vertical velocity prediction for the BS, FD 2-D models for a horizontal shortening rate of 4 mm yr^{-1} for a 30° and 60° dipping fault locked down to 10 km depth.

Figs 4(e)–(h) compare the prediction of the BS and FDR models for a fault locked to a depth of 5 km. Although both models predict a bell-like shape for the horizontal velocity profile close to the fault, the predicted magnitude for the maximum velocity is different and this difference is larger for steeper fault.

Finally, Figs 4(i)–(l) show the effect of adding a slipping patch at the otherwise locked fault. The slipping patch introduces a bell-like shape perturbation to the surface velocity profile, now shifted from the fault trace at the surface. The width of the velocity perturbation depends on the length and depth of the slipping patches. Narrow bell-like shapes found in our PS-InSAR observation are likely to be fitted by variable slip along the fault. We also see that allowing variable slip at the ramp will result in little sensitivity of surface displacement on the dip of the fault. Indeed, the same bell-like shape can be reproduced either by smaller or deeper slip on a steep fault or by larger and shallower slip on a shallow fault.

To conclude, Fig. 4 shows that the BS approach is not suitable for modelling vertical rates away from the fault since it introduces a spurious step in the far-field (Segall 2010). Therefore, this type of modelling is not suitable for modelling InSAR data, because the LOS might include a significant contribution from the vertical component. Fig. 4 also shows that the predicted horizontal profile differs between the BS and FD models. This difference increases with steeper dip. Especially, the BS approach predicts that the surface displacement in the direction perpendicular to the fault trace close to the fault can exceed the far-field value, a pattern not predicted for the FD and FDR models.

4.5 Bayesian exploration of searched parameters

We use a Bayesian approach to rigorously evaluate the resolution of parameters and sample different models allowed by the data. Our observations of fault perpendicular velocities denoted d, are related to the vector of unknown m including slip and fault geometrical parameters through the functional g by $g(m) = d$. Because the vector m includes geometrical parameters, $g(m)$ is a nonlinear function. In Bayesian approaches, the *a priori* information about the searched parameters is combined with the observations to derive posterior probabilities of the searched parameters. The *a posteriori* probability density function (PDF) of the model m given the data d is $\rho(m|d) \propto \rho(d|m)\ \rho(m)$, where $\rho(m)$ is the *a priori* PDF on model parameters m and $\rho(d|m)$ the likelihood PDF of d given m given by $\exp(-1/2(d\text{-}g(m))^{\mathrm{T}} C_D{}^{-1}(d\text{-}g(m)))$ with C_D being the covariance matrix on the data d. Since the data covariance estimation was conservative (underestimation), the confidence intervals of the model parameters are also underestimated.

We use the PyMC library (Patil *et al.* 2010) which implements a Metropolis algorithm to explore the posterior PDF. For all models, we used 500 000 initial samples, rejecting the first 100 000 samples to minimize the effect of the initial model, and decimate the resulting samples by a factor of 10.

4.6 2-D inversion from GPS data

In a first approach, we test the BS and FD approaches using the GPS results only. The searched parameters for the BS models are the horizontal shortening rate V_h, the dip, the locking depth H and the location of the fault trace at the surface (xf). The applied backslip equals to V_h/cos(dip) (Fig. 5c). For the FD model, the searched parameters are V_h, the depth of the décollement H and the horizontal location of the décollement tip (Fig. 6c). The input data are the horizontal velocities projected along 4 profiles perpendicular to the fault segment (Fig. 2) where GPS data are dense enough. The fault strike is changing from north to south, hence we choose to angle the profiles to cut perpendicularly the fault and follow the GPS pattern. For both BS and FD models, we use a uniform prior in the interval of 0–10 mm yr^{-1} for the shortening rate, and 0–15 km for the locking depth and ∼10 km of possible offset with respect to the fault trace. For the BS model, we use an interval of 5°–85° for the dip. To increase the number of observations to resolve the searched parameters, profiles are inverted simultaneously sharing the same value of dip and shortening rate V_h. We assumed different values of locking depth or depth of the decollement H (H_1, H_2, H_3, H_4) for the four profiles as it is obvious that the velocity gradient across the fault is different among profiles. Similarly, the location of the fault is solved independently for each profile, by taking different values of xf (xf_1, xf_2, xf_3, xf_4) to reflect the variable location of the different segment with respect to our reference point.

We find that GPS site PLHA located on the Pululahua Volcano (Fig. 1b) and used in the northernmost profile (profile 1) appears as being an outlier in many models. Therefore, PLHA has been removed from the inversions. Figs 5(b) and 6(b) show some of the components of the posterior PDF together with the fit achieved to the data for the mean model (Figs 5a and 6a). Both the BS and FD approaches provide good fit to the data (wrms = 0.51 and 0.44 mm yr^{-1} for the BS and FD model, respectively, Figs 5a and 6a). The shortening rate V_h is consistently found to be in the range of 3.1–3.5 mm yr^{-1} at the 68 per cent confidence level. We find that the locking depth is less than 1.3 km for profiles 2 and 3 in central Quito. Larger locking depths are found for the northern and southern segments (profiles 1 and 4). For the BS model, the preferred (Maximum A Posteriori, MAP) dip is very steep (∼65°) but both the mean and median models provide estimates around 45° with comparable misfit to the data.

Although both the BS and FD models could achieve a good fit of GPS observations and demonstrate a very small elastic strain accumulation at the Quito fault, we suspect that these results are not physically realistic and could bare to unrealistic slip deficit estimates. Indeed, for such models, the elastic strain would accumulate only within the very shallowest part of the fault (∼1 km), which is mostly made of unconsolidated material for which inelastic deformation is likely to occur.

4.7 Joint GPS-InSAR based models

In a second step, we include the InSAR data. One of the main patterns in the InSAR map is the 5 km narrow bell-like shape of LOS

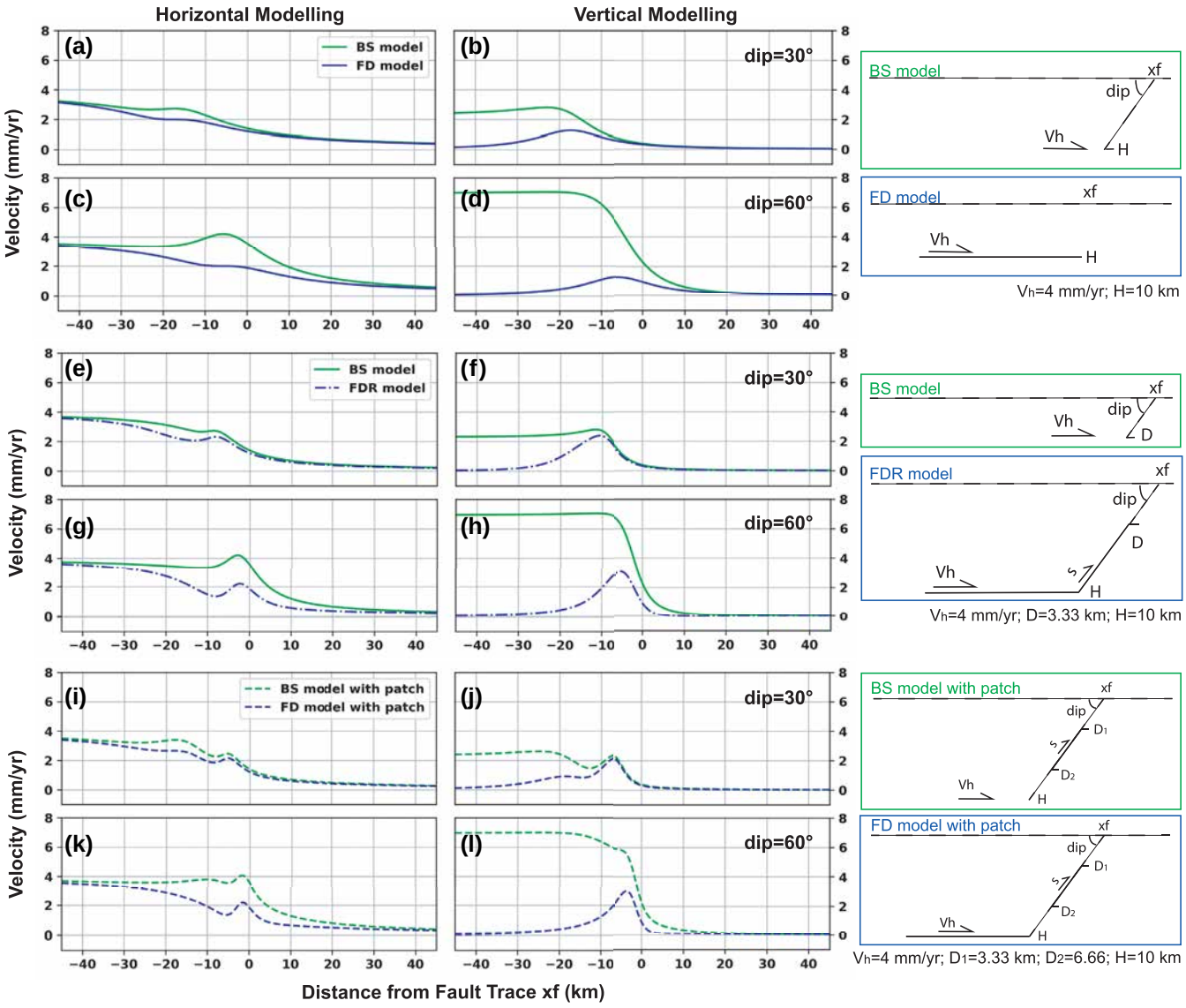

Figure 4. Comparison between horizontal and vertical velocity predictions for 2-D synthetic elastic models. All models are for a shortening rate of 4 mm yr^{-1}, and a locking depth down to 10 km depth. Velocity predictions are shown for a dip of 30° or 60° as indicated in the middle column subplots. The right column shows the model setting and parameters for the back-slip (BS), flat décollement (FD) and flat décollement-ramp (FDR) models. The fault is in solid line when slipping and dashed line when locked. xf corresponds to the location of the fault at the surface, or in the case of the FD model, the surface location of the decollement tip. xf = 0 on the *x*-axis for model predictions.

rate found for the central Quito basin along profile 2 and 3 (Fig. 7a). None of the previous models explored can explain this pattern, but the synthetic tests described in paragraph 4.1 suggest that flat décollement-ramp models can reproduce this shape of signal. For the FDR model, two parameters are added with respect to the FD model: the dip of the ramp and top depth of the ramp. We find that if we leave all parameters free, that is having a uniform prior, the FDR model tends to choose values for the décollement depth (H) of the order of ∼2 km, providing similar results to the FD models. To force a more comprehensive exploration of the models allowed by the data, we run several inversions fixing the décollement depth at 3, 5, 7 and 10 km. For InSAR data, corrections for an offset and a tilt along the profile direction are estimated. The InSAR profiles are decimated using a median filter. We exclude profile 4 from these inversions because the residual signal in the InSAR data southwest of the Ilalo Volcano cannot be fitted by a simple geometry with one single fault (see discussion).

For these models, we find that a décollement depth of 7 or 10 km with shallow (2–4 km) locking depth on the ramp can simultaneously fit the GPS and InSAR data. We find that there is little sensitivity to the dip because similar good fit is achieved for values of 10°–50° (with slightly preferred values of 30°–35°) for profiles 1 and 3. For profile 3 in central Quito, the narrow bell-like LOS pattern is better fitted with a single slipping patch at 2–4 km depth on a ramp with a dip in the range of 20°–35° (Fig. 7). The FDR models reveal a wider range of horizontal shortening rate from 3 to 5 mm yr^{-1} allowed by the data.

In summary, the results from the 2-D tests show that (1) the horizontal shortening rate accommodated across the Quito fault is in the range of 3–5 mm yr^{-1}; (2) fitting GPS data with a simple flat

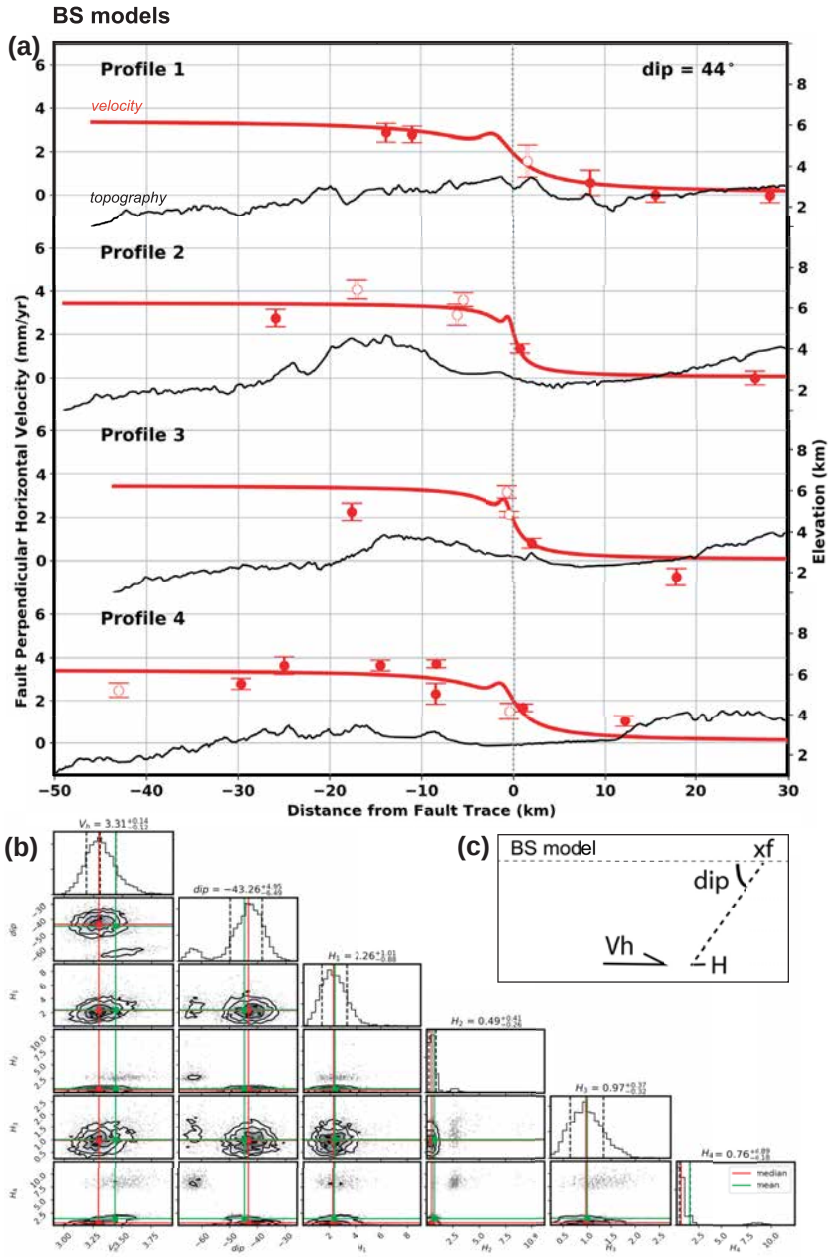

Figure 5. Results from the Bayesian inversion using GPS data only and the back-slip (BS) model along profiles crossing the Quito fault. Location of the profile are shown in Fig. 2. (a) Red curves are model prediction from the mean model for the along profile horizontal velocity. Circles filled in red are survey mode GPS whereas circles filled in white are continuous GPS. Black line shows the topography. (b) One- and 2-D posterior PDF for the following parameters: the shortening rate (V_h), the dip and the four locking depths associated with each profile (H_1, H_2, H_3 and H_4). (c) Schematics Model of a BS with the parameters used for the inversion: dip; xf, location of the fault on the surface; V_h, shortening rate; H, locking depth.

décollement or with back-slip models provides a very shallow locking depth but cannot explain the bell-like shape of InSAR LOS rate (Figs 4a and c); (3) simultaneously fitting the sharp gradient seen in both the GPS velocities and InSAR LOS rates requires shallow creep to occur along a ramp; and (4) the amount of shallow creep along the ramp appears to be variable along strike with maximum aseismic slip occurring along the central Quito segment of the fault.

4.8 3-D spatial variable interseismic models

In the models of Section 4.7, the shallow creep is modelled using a single creeping patch along the ramp, with the model build-in condition that the slip rate is constant along the patch. This is certainly a crude approximation since slip is likely to vary both along dip and along strike at the fault plane. To obtain a more realistic model of the shallow creep distribution, we design a 3-D inversion of spatially variable slip at depth. Our model follows the approach by Daout *et al.* (2016a). The block-like far-field velocity is modelled using a 110 × 110 km^2 horizontal dislocation at depth H slipping at velocity V_h. This length embeds the whole Quito fault system along strike (60 km) and also enables modelling of the PS-InSAR gradient seen north and south of the Quito fault. The width ensures a block-like behaviour for the far-field GPS data. The horizontal dislocation connects to a ramp reaching the surface

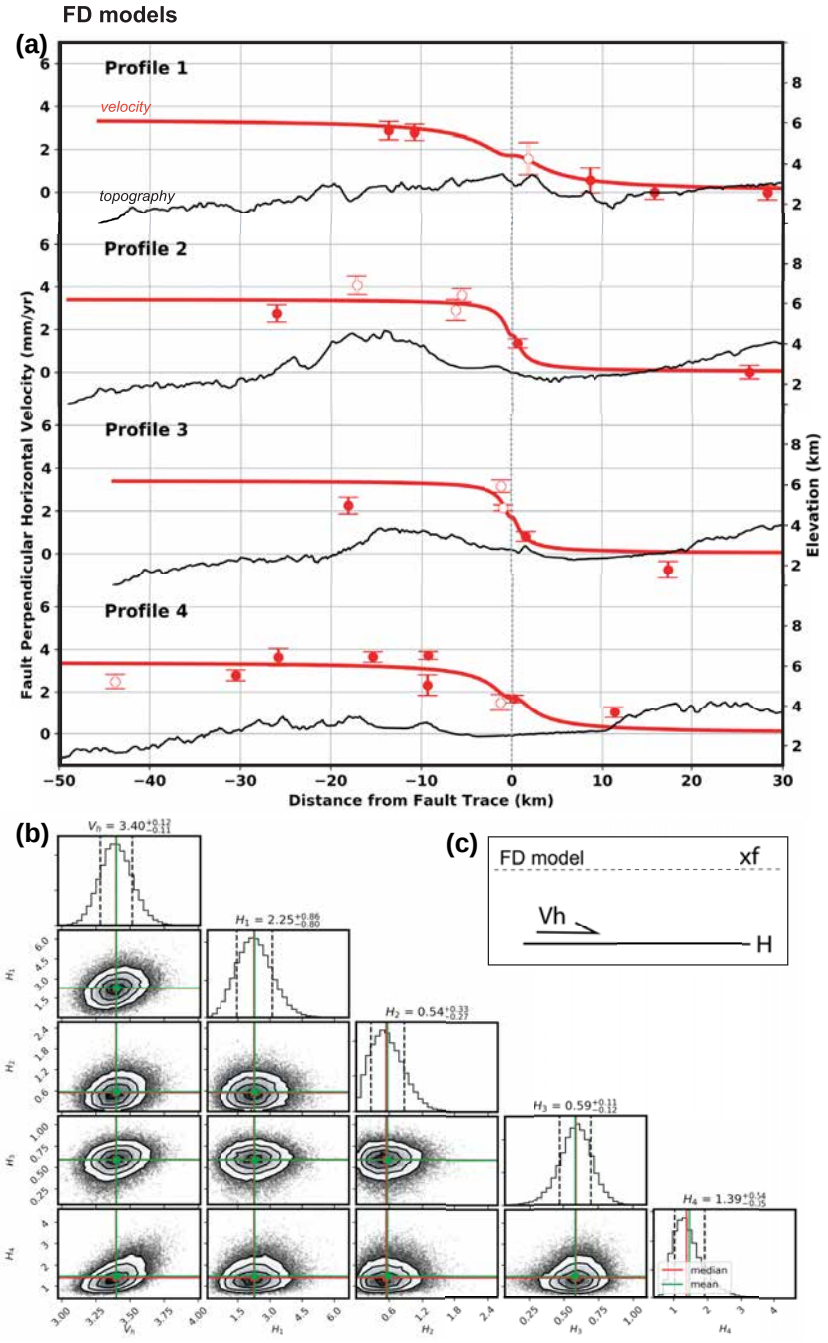

Figure 6. Same as Fig. 5 but with a Flat Décollement (FD) model.

along the fault trace in the central segment (Figs 8 and S1). We discretize the ramp into 2×2 km^2 subfaults. The surface fault trace is simplified by a single plane with a fixed strike of 200° that follows the foot of the main escarpment in the central part of the fault where more data are available to constrain the shallow behaviour of the fault.

Once V_h and the geometry are chosen, solving for spatially variable slip along the ramp is a linear inverse problem. We use the stochastic inversion approach described in Nocquet (2018) to solve for slip at each individual subfault under the condition that the slip must be positive and lower or equal to V_h/cos(dip) in the shortening direction. This condition implicitly enforces that the observed deformation is not transient since it does not exceed the slip imposed by the far-field horizontal shortening rate. We use a regularization condition in the form of a penalty function $(m–m_0)^{\mathrm{T}}{C_m}^{-1}(m–m_0)$, where C_m is a covariance matrix of the form of $Cm = \sigma * 2 * \exp(-r_{ij}/rc)$ with sigma being the constraint to the *a priori* model m_0, r_{ij} the distance between subfault i and j and rc a critical distance controlling the correlation between subfault slips. Because our simple geometry does not account for slight change in strike between different segments, we allow the rake to vary around 106° by setting a sigma value of 1 mm yr^{-1} on the conjugate component of slip at

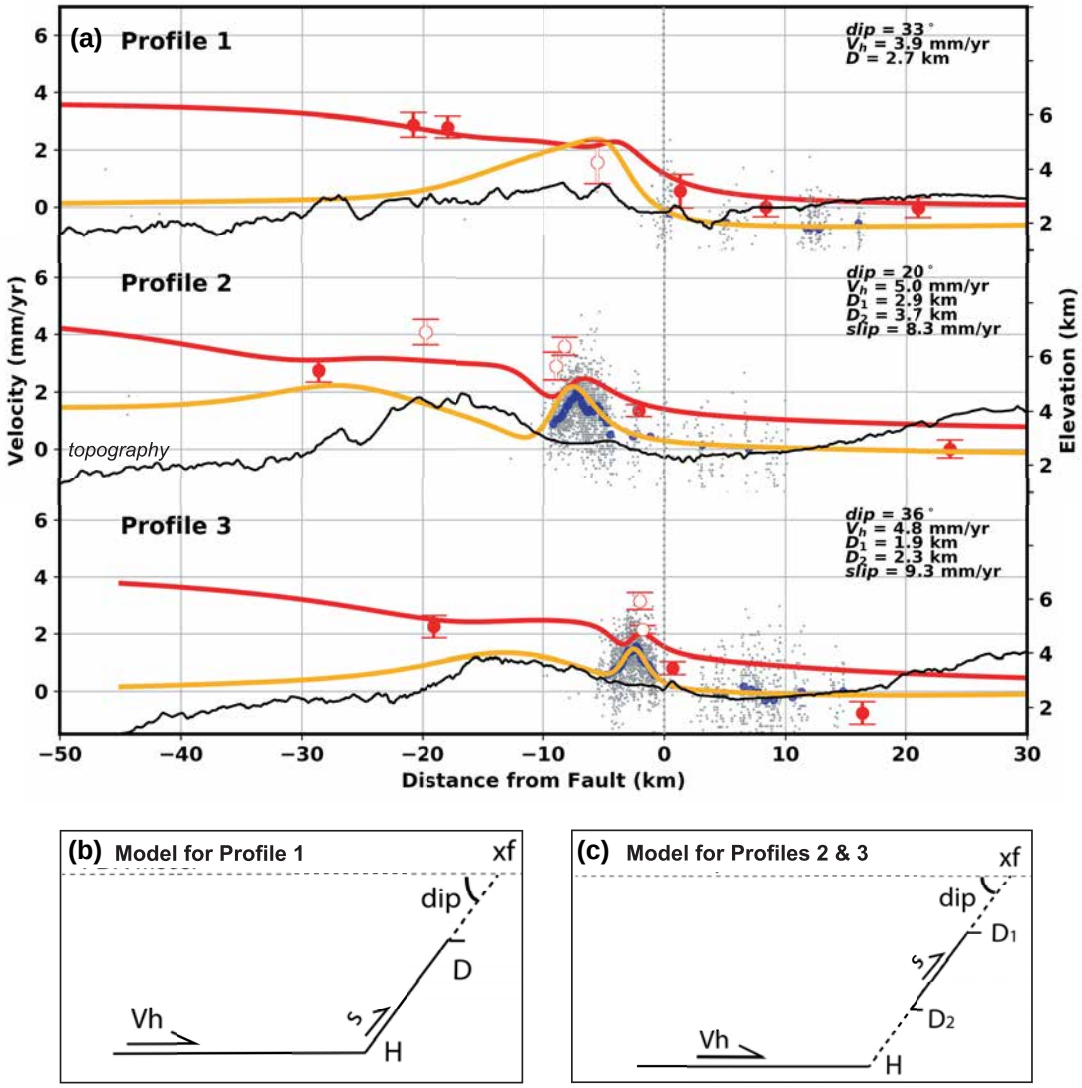

Figure 7. Results of the Bayesian inversion using GPS and InSAR data and the Flat Décollement Ramp (FDR) model with a décollement depth at 10 km. a) Red curves are along profile horizontal velocity model prediction from the mean model. Orange curves are model prediction from the mean model along the LOS. Light grey dots are LOS rates along a 400 m wide swath around the profile location. Blue circled are the selected points from the LOS velocity data used in the inversion a median filtered. Red filled circles indicate survey mode GPS whereas white filled circles are continuous GPS. Black line shows the topography. b) & c) Schematic models of a Flat Décollement Ramp (FDR) and a Flat Décollement (FD) with a slipping patch, with the parameters used for the inversion: dip; xf, location of the fault on the surface; V_h, shortening rate; D, locking depth (or D_1–D_2: patch of the locking depth); H, décollement level; s, slip on the ramp.

each subfault. Because InSAR data might be subject to systematic long wavelength errors, we also solve for an overall constant and a tilt of the LOS rates simultaneously to the two components of slip at each subfault.

We perform a grid search for V_h in [3.0, 4.5, 6.0, 8.0] mm yr^{-1}, dip in [20, 30, 40, 50] degrees, and depth in [7, 10, 13] km. For each V_h, dip and depth, we solve for both $m_0 = 0$ and $m_0 = V_h/\cos(\text{dip})$ with a constraint of 1 mm yr^{-1} and a critical distance *rc* of 4 km. Solving with a prior of $m_0 = 0$ provides a minimum slip rate solution, that leads to a maximum moment deficit rate model, while using $m_0 = V_h/\cos(\text{dip})$ provides a maximum slip rate solution, that is a minimum moment deficit rate model.

The 3-D modelling confirms some of the results from the profile analysis. A horizontal shortening $V_h = 8$ mm yr^{-1} overestimates the few far-field GPS data (Fig. S1) while $V_h = 3$ mm yr^{-1} underestimate them. The best agreement for far-field data is found for $V_h = 4.5$ mm yr^{-1} but some models with $V_h = 6$ mm yr^{-1} are also allowed by the data.

As for the 2-D models, our parameter exploration shows little sensitivity to the dip of the fault. For all models tested, a dip value of 50° provides underestimated magnitude for GPS velocities in the central Quito area. Otherwise, dip values from 20° to 40° are acceptable, with best fit achieved for dip values of 20° and 30°. Similarly, the three depths tested [7, 10, 13] km provide comparable fit to the data.

In terms of slip distribution, all models find shallow slip along the fault plane possibly reaching the surface in the central segment, decreasing north and south, as the gradient of the InSAR LOS rate and GPS, when available, become smoother (Figs 8 and S1). The length of the creeping segment is found to be ∼20 km. Its downdip

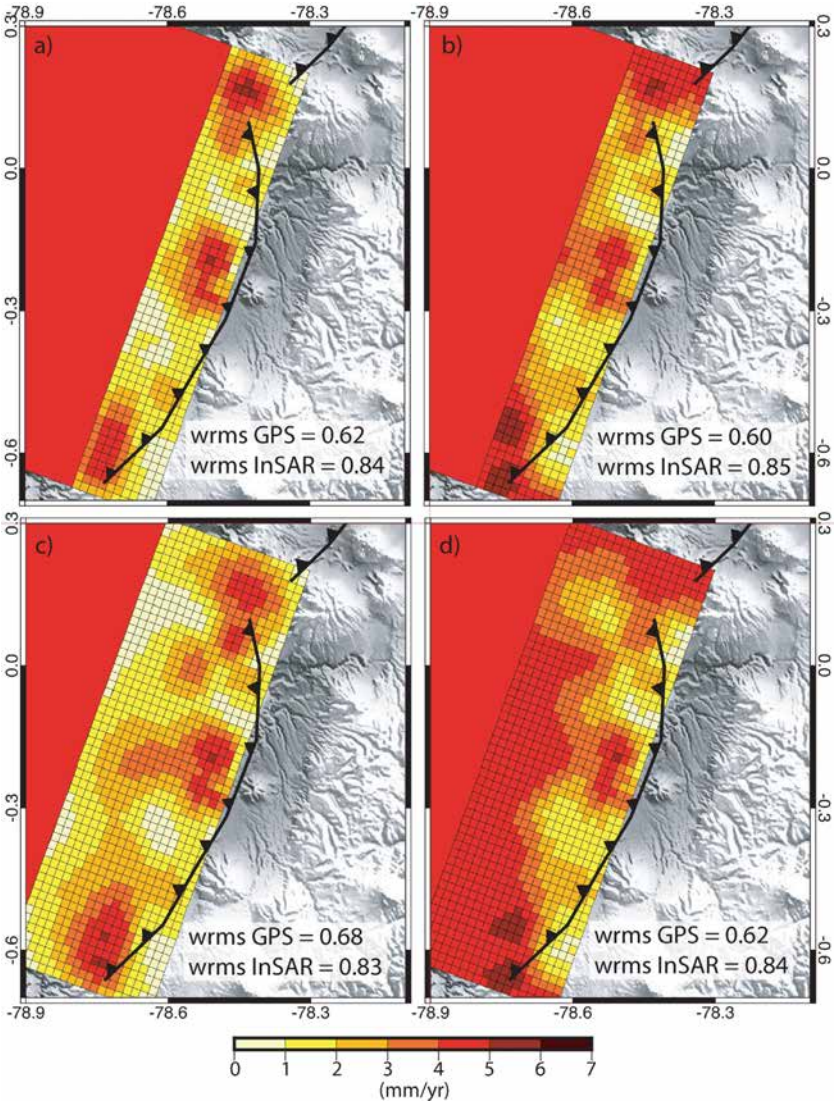

Figure 8. Selection of four different fault slip models along the Quito Fault System**.** Fault dipping at 20° with a shortening rate between 4.6 and 4.9 mm yr^{-1} and a flat décollement at either at 7 km depth (a and b) and 13 km depth (c and d). a) and c) have a prior $m_0 = 0$ (minimum slip rate solution). b) and d) have a prior $m_0 = V_h/\cos(\text{dip})$ (maximum slip rate solution). The values are in mm yr^{-1} and colour-coded according to the scale shown at the bottom. The barbed black line shows the simplified surface trace of the fault. Fit to the data are shown in Fig. S1.

extent is at least 5 km and some models find that the whole ramp is creeping along the central segment. Minimum slip models highlight two additional areas of slip at the southern and northern tip of the fault plane, but their extents are poorly constrained by spatially scarce data.

Overall, the size of the creeping areas, and notably their extension at depth, largely depends on the chosen *a priori* model. In some models, almost the whole fault is found to be creeping at a rate close to the one imposed by the far-field shortening. The areas of our idealized fault that are not creeping correspond to areas where the fault trace is located a few kilometres west of the modelled fault trace (Figs 8 and S1). Therefore, those models indicate the possibility that the Quito fault might be almost entirely creeping. Alternatively, models with minimum slip prior show the possibility that shallow creep is restricted to the first shallowest kilometres of the fault and that significant coupling occurs north and south of the central segment.

5 DISCUSSION

5.1 Comparison with the seismicity depth distribution

Our preferred models include a flat décollement at a 10 km depth that connects to a ramp reaching the surface. Rather than a realistic description of the fault geometry at depth, such a model provides a first order approximation of the depth transition between ductile processes and elastic strain build-up. The depth of such a transition can independently be assessed by looking at the distribution of seismicity as a function of depth. Fig. S3 shows the depth distribution of earthquakes in the Quito area, using the IG-EPN instrumental earthquake catalogue (https://www.igepn.edu.ec/red-nacional-de-sismografos). The IG-EPN earthquake catalogue covers the 2011–2018 period using the data from the national Ecuadorian permanent network (Alvarado *et al.* 2018). When considering earthquakes with magnitude M_L above 2, the depth distribution is confined within the first 10 km (Fig. S3). Although this distribution indicates that small

earthquakes occur in a volume rather than being located on a single fault plane, the seismogenic depth derived from our inversion is consistent with the observed depth distribution of earthquakes.

5.2 Comparison with fault morphology

Morphology of fault related anticlines is also an indicator of the fault geometry at depth. Despite some variability among modelling approaches, models of fold evolution usually predict that the width of the fold roughly scales with the depth of the root of the underlying causative fault (e.g. Savage & Cooke 2003; Bernard *et al.* 2007; Johnson 2018). If true, for the Quito fault, the characteristic width of the different segments is about 7 km, a value also consistent with our modelling results and the seismicity distribution with depth. Such a relatively thin seismogenic layer might be due to the thick (50–60 km, Reguzzoni *et al.* 2013; Araujo 2016) crust documented beneath the Andes, therefore inducing a larger radiogenic thickness, relatively high heat flow and hence thin elastic thickness. The Inter-Andean valley in Ecuador is the *locus* of significant quaternary volcanic activity, and small volcanoes (Fig. 1b) attest for magmatic intrusion reaching the surface. Therefore, the crust in the Quito area might be locally hot, therefore reducing the thickness of its elastic part.

5.3 Overall slip deficit moment rate and implication for seismic hazard

The existence of an active fault poses a serious hazard to the growing city of Quito and its surroundings, especially considering that even moderate-size earthquakes have generated significant damages in the past. Within our present-day understanding of the earthquake cycle, significant creep reduces the accumulation of slip deficit at faults, then reducing the amount of elastic energy available for earthquakes. Although creeping faults recorded earthquakes up to magnitude 6.6 and possibly even larger events (Harris 2017), earthquakes should, however, be less frequent at creeping segments than at their locked counterparts for the same slip rate and size. Under the assumption that the observed creep is steady through time and that the slip deficit is a first order indicator of the moment available for earthquakes, we can perform simple calculations. For all 3-D models explored, we can estimate the slip deficit at each subfault as the difference of the maximum slip rate provided by V_h/cos(dip) and the inverted slip rate. We integrate it over the fault area and we calculate a rate of moment deficit accumulation over the whole fault. For this calculation, we remove subfaults found with no slip that are located east of the known surface fault trace that would otherwise contribute to the slip deficit estimates. Such procedure roughly reduces by 30 per cent the maximum moment rate deficit. Given the fact that we have inverted both for the maximum and minimum slips, the range of moment deficit rate is considered to reflect the amount of moment deficit accumulation rate allowed by the data. Taking the results from the most extreme models, our spatially variable slip inversions are equivalent to 20–80 per cent of the average interseismic coupling along the fault. Under these assumptions, we find a moment deficit accumulation rate along the Quito fault to have a lower bound value of 0.3×10^{17} N.m.yr^{-1} and an upper bound value of 1.9×10^{17} N.m.yr^{-1}. These values are equivalent to a single M_w 6.7–7.3 earthquake every 500 yr, a magnitude possible given the length of the fault (∼60 km).

In order to provide a more realistic description of earthquake recurrence, we use the geodetic moment accumulation rates to derive a cumulative exponential-truncated Gutenberg–Richter distribution (G-R, form 2 in Anderson & Luco 1983). Both a b-value and an estimate of the maximum magnitude that the fault can generate must be assumed. Beauval *et al.* (2014) derived a magnitude–frequency distribution for the Quito fault system (Fig. S4a), which is not well constrained due to the low number of events above M_w 4.5 in the area. Nonetheless, we compare our results to this catalog-based recurrence model. Applying Leonard (2010) scaling relationship for reverse events, a 90–100 km long and 20 km width fault corresponds to a magnitude of M_w 7.3. Assuming the same *b*-value and an M_{max} value of 7.3, we find that the geodetic-based G–R from the lower moment deficit accumulation requires an *a*-value lower than the one from seismicity rates, while the geodetic-based G–R from the larger moment deficit accumulation requires an *a*-value higher than observed from seismicity rates (Fig. S4a). For earthquakes of magnitude larger or equal to 6.5, the geodetic-based models predict a mean interevent time between 200 and 1100 yr, depending on the model chosen. We also determine the lowest maximum magnitude required so that the yearly seismic moment calculated from the integration of the G–R curve equates the yearly moment deficit accumulation. To make the lower geodesy-based and seismicity-based rates consistent, a smaller M_{max} of 6.8 is required (Fig. S4b), predicting a mean interevent time between 150 and 900 yr for an event $M_{max} \geq 6.5$.

Our results further highlight a segmentation of the slip deficit accumulation along the Quito fault, made of two segments accumulating strain separated by the 20-km-long creeping segment in central Quito. While our model exploration shows that creep or locked behaviours are both possible at depth, our results highlight that the central segment is creeping along its shallow part, at least down to 5 km. An open question, as documented for subduction megathrusts, is to know whether this creeping segment could act as a barrier to the seismic rupture propagation. In this perspective, future earthquake scenarios for Quito could include the possibility of more frequent 30-km-long ruptures occurring at the northern and southern segments than in the central part.

5.4 The 1995–1996 transient motion—a fold growth pulse?

Our PS-InSAR time-series highlight a transient deformation, clearly seen for the interferograms spanning the 11 April 1995–24 October 1996, period (Figs 3d and h). It occurred southeast of the Ilalo Volcano, a few kilometres east of the main surface trace of the Quito fault in a semi-urban area. This transient signal has a LOS magnitude of ∼20 mm with a radial pattern over ∼4 km. The LOS rate map for the 1996–2000 period further shows a similar pattern at a smaller amplitude (1 mm yr^{-1}) and smaller length-scale (1 km, Fig. 3f), indicating that deformation in this area persisted with a lower intensity during the 7 yr of InSAR observation. The location of this signal correlates with a previously identified active Conocoto fold located east of the main Quito Escarpment at long. −78.47°, lat. −0.29° (Fig. 9). The Conocoto fold is a 1.5-km-long, 800-m-wide and 100-m-high structure. Its recent activity is attested by the deflection of the river course and it has been interpreted as a young growing fold induced by a secondary propagating west dipping thrust fault (Fig. 9c and Alvarado *et al.* 2014). Because of the observed radial pattern of deformation and the absence of negative LOS displacement, such a signal is unlikely to be modelled using reverse slip along an elastic dislocation. We speculate that this transient deformation signal arises from the ductile deformation of the top layers induced by local aseismic slip along the underlying

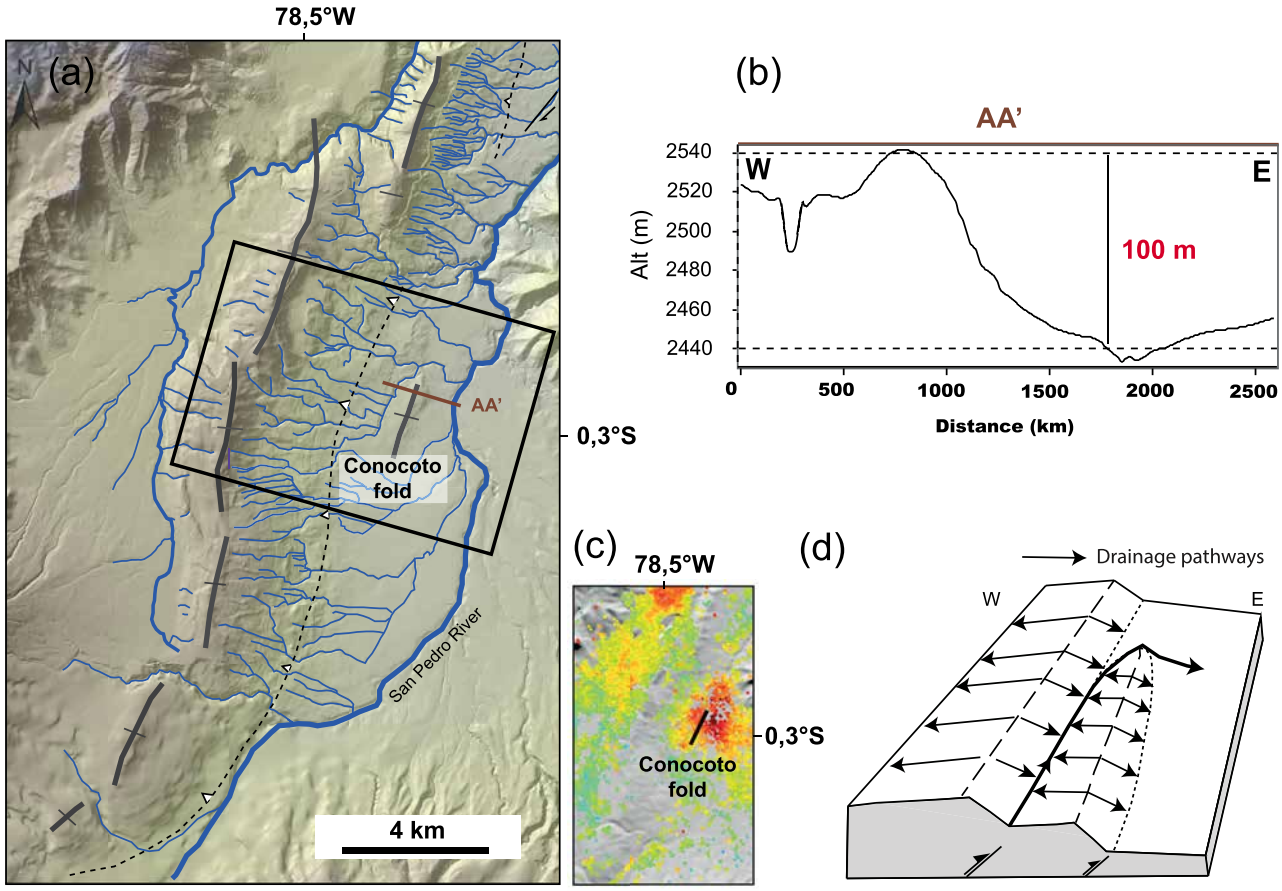

Figure 9. (a) Drainage map on the Inter-Andean valley, east of the Quito Basin and neoctectonic interpretation (modified from Alvarado 2012). (a) Blue curves are rivers; thick black lines are the top fold locations and the dashed black line with triangles is the surface location of the main thrust fault. Note the deflection of the drainage system to the north around the Conocoto fold. Black rectangle is the location of the inset (b) and (d). (b) Topographic profile across the Conocoto fold. (c) Same area as in a) with the LOS surface velocity from Fig. 3(a) compared with the location of the Conocoto fold. (d) Propagation model of thrust (inspired from Jackson *et al.* 1996).

fault. If we interpret the LOS displacement as being mainly vertical, this implies a steady uplift rate of ∼1 mm yr^{-1} calculated for the 1993–1995 and 1996–2000 periods. The LOS displacement is ∼20 mm during the 1.5 yr separating the two SAR acquisitions (from 1995/4/11 to 1996/10/23), but we do not know when the uplift took place during this period. Nonetheless, the InSAR results indicate that the uplift rate accelerated by a factor of at least 20 with respect to the uplift rate before April 1995 and after October 1996. This fold growth pulse accounts for 70 per cent of the finite displacement over the 1993–2000 period. Although longer measurements are required to know how frequent are these events, it suggests that fold growth pulses can contribute significantly to the building of fold topography.

6 CONCLUSIONS

We have derived a high spatial resolution interseismic surface velocity field from GPS data and PS-InSAR analysis around the Quito reverse fault system, directly threatening a highly populated area of the northern Andes. We find that the Quito fault accommodates 3–5 mm yr^{-1} of horizontal shortening. As a whole, relatively sharp gradients across the Quito fault highlight a weak rate of elastic strain accumulation and a shallow (<3 km) locking depth. The central segment shows the sharpest velocity gradient, providing evidence of aseismic slip taking place at shallow depth along the fault plane and possibly reaching the surface, while segments north and south of it possibly hosts larger slip deficit accumulation rates. Aside these trends, the details of interseismic coupling distribution appear to be model dependent. In particular, some models including a flat décollement and a ramp allow for slip deficit to accumulate at depth. Overall, our results demonstrate that strain accumulation is spatially heterogeneous along the Quito fault. The observed shallow aseismic slip concurs to confirm that a significant percentage of crustal faults on Earth may be creeping at shallow depth (Harris 2017). In terms of seismic hazards for the Quito area, our results help to refine previous estimates of earthquake time recurrence (Beauval *et al.* 2014, 2018). Our estimates for the rate of moment deficit accumulation derived from a 3-D spatially variable interseismic coupling translate into recurrence time for magnitude 6.5 + earthquake to be between 200 and 1100 yr, a value consistent or slightly lower than proposed in previous studies (Beauval *et al.* 2014, 2018; Parra *et al.* 2016).

Finally, we identify a transient deformation signal related to the development of a secondary fold, a few kilometres east of the main fault trace. This observation suggests that fold growth might result from pulses of accelerated deformation, possibly driven by slow slip events occurring along the fault plane underlying the soft top layers experiencing anelastic deformation. On the overall, our results

Table 1. GPS velocities with respect to our stable fault foot wall block reference frame (see Section 2.1). Longitude, latitude in decimal degrees; Ve, Vn: east and north components of velocity in mm yr^{-1}; SVe, SVn: formal error (1σ confidence level) of Ve, Vn.

Sites	Long.	Lat.	Ve	Vn	SVe	SVn
01AQ	−78.498	− 0.147	3.49	1.16	0.35	0.43
ANTN	−78.162	− 0.463	0.27	0.57	0.23	0.25
ANTS	−78.170	− 0.497	− 0.04	0.28	0.29	0.23
CASI	−78.480	− 0.037	2.50	0.24	0.52	0.66
CATE	−78.428	0.000	1.72	− 0.55	0.40	0.53
CORE	−78.524	− 0.328	2.06	− 0.63	0.34	0.44
CULA	−78.696	0.144	3.31	1.77	0.29	0.35
EPEC	−78.446	− 0.315	1.12	− 0.95	0.25	0.49
GGPA	−78.593	− 0.180	4.74	0.38	0.32	0.19
HSPR	−78.850	− 0.352	2.57	0.68	0.24	0.21
IGNA	−78.752	− 0.451	2.60	− 0.37	0.18	0.23
ILAL	−78.419	− 0.263	1.60	0.18	0.13	0.16
JERU	−78.358	− 0.006	0.70	0.56	0.24	0.31
LACH	−78.420	0.161	1.19	0.38	1.33	1.64
MIRA	−78.509	− 0.270	3.24	− 1.66	0.13	0.16
NAYO	−78.436	− 0.157	2.02	− 0.05	0.15	0.21
NONO	−78.599	− 0.042	3.57	0.86	0.26	0.32
OYAM	−78.329	− 0.203	0.38	0.07	0.28	0.34
PAM1	−78.209	− 0.080	0.62	0.66	0.23	0.38
PAPA	−78.141	− 0.381	0.03	0.78	0.10	0.52
PINT	−78.356	− 0.420	0.69	− 0.74	0.18	0.17
PLHA	−78.502	0.022	4.15	1.27	0.15	0.21
QUEM	−78.497	− 0.237	4.27	− 0.50	0.21	0.11
QUI1	−78.494	− 0.215	3.30	0.15	0.09	0.49
UNGU	−78.557	− 0.237	3.26	− 1.24	0.18	0.23
LUMQ	−78.471	− 0.216	1.95	− 0.16	0.16	0.21
PAL0	−78.649	− 0.219	3.33	− 0.97	0.28	0.36
18AQ	−78.489	− 0.185	4.22	0.91	0.23	0.41
SALF	−78.155	− 0.233	1.13	− 0.23	0.23	0.18

emphasize a dominant contribution of aseismic processes for the Quito fault system.

ACKNOWLEDGEMENTS

We thank two anonymous reviewers for their thorough reading of the manuscript and comments that greatly helped us to improve the article. This research was supported by the French *Agence National de la Recherche* (ANR) through the project REMAKE (2016–2019, Grant Number ANR-15-CE04-004), and by the *Institut de Recherche pour le Développement* (IRD), the Geophysical Institute in Quito, part of the Escuela Politecnica Nacional, and ISTerre and Géoazur laboratories. InSAR data were processed thanks to an IRSN and CNES funding (2012–2014). We are grateful to R. Grandin for insightful discussions. This work has been carried out in the frame of the Joint International Laboratory '*Seismes & Volcans dans les Andes du Nord*' (LMI SVAN).

REFERENCES

Altamimi, Z., Rebischung, P., Métivier, L. & Collilieux, X., 2016. ITRF2014: a new release of the International Terrestrial Reference Frame modeling nonlinear station motions: ITRF2014. *J. geophys. Res.*, **121,** 6109–6131.

Alvarado, A., 2012. Néotectonique et cinématique de la déformation continentale en Equateur. *Sciences de la Terre*. Université de Grenoble, Français.

Alvarado, A. *et al.*, 2014. Active tectonics in Quito, Ecuador, assessed by geomorphological studies, GPS data, and crustal seismicity. *Tectonics,* **33,** 67–83.

Alvarado, A. *et al.*, 2016. Partitioning of oblique convergence in the Northern Andes subduction zone: migration history and the present-day boundary of the North Andean Sliver in Ecuador: eastern limit of the North Andean Sliver. *Tectonics,* **35,** 1048–1065.

Alvarado, A. *et al.*, 2018. Seismic, volcanic, and geodetic networks in Ecuador: building capacity for monitoring and research. *Seismol. Res. Lett.,* **89,** 432–439.

Anderson, J. G. & Luco, J. E., 1983. Consequences of slip rate constraints on earthquake recurrence relations. *Bull. seism. Soc. Am.* **73**(2), 471–496.

Araujo, S., 2016. Travel time tomography of the crust and the mantle beneath Ecuador from data of the national seismic network, *PhD thesis*, Institut des Sciences de la Terre, Université Grenoble Alpes, Grenoble, France.

Baby, P., Rivadeneira, M., Barragan, R. & Christophoul, F., 2013. Thick-skinned tectonics in the Oriente foreland basin of Ecuador. *Geol. Soc. Lond., Spec. Publ.,* **377**(1), 59–76.

Baize, S. *et al.* 2015. Paleoseismology and tectonic geomorphology of the Pallatanga fault (Central Ecuador), a major structure of the South-American crust. *Geomorphology,* **237,** 14–28.

Beauval, C., Yepes, H., Bakun, W.H., Egred, J., Alvarado, A. & Singaucho, J.-C., 2010. Locations and magnitudes of historical earthquakes in the Sierra of Ecuador (1587-1996). *Geophys. J. Int.,* **181**(3), 1613–1633.

Beauval, C. *et al.*, 2013. An earthquake catalog for seismic hazard assessment in Ecuador. *Bull. seism. Soc. Am.,* **103,** 773–786.

Beauval, C., Yepes, H., Audin, L., Alvarado, A., Nocquet, J.-M., Monelli, D. & Danciu, L., 2014. Probabilistic seismic hazard assessment in Quito, estimates and uncertainties, *Seismol. Res. Lett.* **85**(6), 1316–1327.

Beauval, C. *et al.*, 2018. A new seismic hazard model for Ecuador. *Bull. seism. Soc. Am.,* **108**(3A), 1443–1464.

Bernard, S., Avouac, J.-P., Dominguez, S. & Simoes, M., 2007. Kinematics of fault-related folding derived from a sandbox experiment, *J. geophys. Res.,* **112,** B03S12.

Champenois, J., Audin, L., Baize, S., Jomard, H., Nocquet, J.-M. & Alvarado, A., 2013. Interseismic deformations along Ecuador active fault systems: contribution of space-borne SAR Interferometry, in *Proceedings of the AGU 2013 Meeting of the Americas*. Mexico, Cancun, 14–17 May.

Champenois, J., Baize, S. & Jomard, H., 2015. Apport des méthodes d'imagerie radar satellitaire pour l'étude des déformations de surface. PRP-DGE/SCAN/BERSSIN. Rapport PRP-DGE n°2015-00019, 1–74.

Daout, S., Barbot, S., Peltzer, G., Doin, M.-P., Liu, Z. & Jolivet, R., 2016a. Constraining the kinematics of metropolitan Los Angeles faults with a slip-partitioning model: slip partitioning in Southern California. *Geophys. Res. Lett.,* **43,** 11 192–11 201.

Daout, S. *et al.*, 2016b. Along-strike variations of the partitioning of convergence across the Haiyuan fault system detected by InSAR. *Geophys. J. Int.,* **205**(1), 536–547.

Dumont, J.F., Santana, E., Valdez, F., Tihay, J.P., Usselmann, P., Iturralde, D. & Navarette, E., 2006. Fan beheading and drainage diversion as evidence of a 3200-2800 BP earthquake event in the Esmeraldas-Tumaco seismic zone: a case study for the effects of great subduction earthquakes. *Geomorphology,* **74,** 100–123.

Egred, J., 2009. Catalogo de terremotos del Ecuador 1541–2009, *Escuela Politecnica Nacional*, Instituto Geofisico, Internal Report.

Floyd, M. A. *et al.*, 2010. A new velocity field for Greece: implications for the kinematics and dynamics of the Aegean. *J. geophys. Res.,* **115**(B10), doi:10.1029/2009JB007040.

Fukahata, Y. & Matsu'ura, M., 2006. Quasi-static internal deformation due to a dislocation source in a multilayered elastic/viscoelastic half-space and an equivalence theorem. *Geophys. J. Int.,* **166**(1), 418–434.

Garcia-Aristizabal, A., Kumagai, H., Samaniego, P., Mothes, P., Yepes, H. & Monzier, M., 2007. Seismic, petrologic, and geodetic analyses of the 1999 dome-forming eruption of Guagua Pichincha volcano, Ecuador. *J. Volc. Geotherm. Res.,* **161,** 333–351.

Guillier, B., Chatelain, J.-L., Jaillard, ., Yepes, H., Poupinet, G. & Fels, J.-F., 2001. Seismological evidence on the geometry of the Orogenic System in central-northern Ecuador (South America). *Geophys. Res. Lett.,* **28,** 3749–3752.

Harris, R.A., 2017. Large earthquakes and creeping faults: large earthquakes and creeping faults. *Rev. Geophys.,* **55,** 169–198.

Herring, T. A., King, R. W., Floyd, M. A. & McClusky, S. C., 2018. *GAMIT Reference Manual, GPS Analysis at MIT, Release 10.70*, Mass. Inst. of Technol.

Hooper, A., Segall, P. & Zebker, H., 2007. Persistent scatterer interferometric synthetic aperture radar for crustal deformation analysis, with application to Volcán Alcedo, Galápagos. *J. geophys. Res.,* **112,** doi:10.1029/2006JB004763.

Hooper, A., 2008. A multi-temporal InSAR method incorporating both persistent scatterer and small baseline approaches. *Geophys. Res. Lett.,* **35**(16), doi:10.1029/2008GL034654.

Jackson, J., Norris, R. & Youngson, J., 1996. The structural evolution of active fault and fold systems in central Otago, New Zealand: evidence revealed by drainage patterns. *J. Struct. Geol.,* **18**(2/3), 217–234.

Johnson, K. M., 2018. Growth of fault-cored anticlines by flexural slip folding: analysis by boundary element modeling. *J. geophys. Res.,* **123,** 2426–2447.

Leonard, M., 2010. Earthquake fault scaling: relating rupture length, width, average displacement, and moment release. *Bull. seism. Soc. Am.,* **100**(5A), 1971–1988.

Lindsey, E.O., Sahakian, V.J., Fialko, Y., Bock, Y., Barbot, S. & Rockwell, T.K., 2014. Interseismic strain localization in the San Jacinto Fault Zone. *Pure. appl. Geophys.,* **171,** 2937–2954.

McCaffrey, R., 2005. Block kinematics of the Pacific–North America plate boundary in the southwestern United States from inversion of GPS, seismological, and geologic data. *J. geophys. Res.,* **110,** B07401.

Meade, B.J. & Hager, B. H., 2005. Block models of crustal motion in southern California constrained by GPS measurements. *J. geophys. Res.,* **110,** B03403.

Mora-Páez, H. *et al.*, 2019. Crustal deformation in the northern Andes – a new GPS velocity field. *J. S. Am. Earth Sci.,* **89,** 76–91.

Morales Rivera, A.M., Amelung, F. & Mothes, P., 2016. Volcano deformation survey over the Northern and Central Andes with ALOS InSAR time series: deformation survey over the Andes. *Geochem. Geophys.,* **17,** 2869–2883.

Mothes, P.A. *et al.*, 2018. Monitoring the earthquake cycle in the Northern Andes from the Ecuadorian cGPS network. *Seismol. Res. Lett.* **89,** 534–541.

Nocquet, J.-M. *et al.*, 2014. Motion of continental slivers and creeping subduction in the northern Andes. *Nat. Geosci.,* **7,** 287–291.

Nocquet, J.-M. *et al.*, 2016. Supercycle at the Ecuadorian subduction zone revealed after the 2016 Pedernales earthquake. *Nat. Geosci.,* **10,** 145–149.

Nocquet, J.-M., 2018. Stochastic static fault slip inversion from geodetic data with non-negativity and bound constraints. *Geophys. J. Int.,* **214**(1), 366–385.

Parra, H., Benito, M. B. & Gaspar-Escribano, J. M., 2016. Seismic hazard assessment in continental Ecuador. *Bull. Earthq. Eng.,* **14**(8), 2129–2159.

Patil, A., Huard, D. & Fonnesbeck, C., 2010. PyMC: Bayesian stochastic modelling in python. *J. Stat. Softw.,* **35**(4), 1–81.

Pennington, W., 1981. Subduction of the Eastern Panama Basin and Seismotectonics of Northwestern South America. *J. geophys. Res.,* **86**(B11), 10 753–10 770.

Pino, D. & Yepes, H., 1990. Apuntes para una historia sismica de Quito. Centro Historico de Quito. Problematica y perspectivas, Direccion de planificaion, Ilustre Municipio de Quito, Ecuador.

Reguzzoni, M., Sampietro, D. & Sansò, F., 2013. Global Moho from the combination of the CRUST2.0 model and GOCE data. *Geophys. J. Int.,* **195**(1), 222–237.

Rolandone, F. *et al.*, 2018. Areas prone to slow slip events impede earthquake rupture propagation and promote afterslip. *Sci. Adv.,* **4,** eaao6596.

Savage, J. C., 1983. A dislocation model of strain accumulation and release at a subduction zone. *J. geophys. Res.,* **88**(NB6), 4984–4996.

Savage, H. M. & Cooke, M. L., 2003. Can flat-ramp-flat fault geometry be inferred from fold shape?: A comparison of kinematic and mechanical folds. *J. Struct. Geol.,* **25,** 2023–2034.

Segall, P., 2010. *Earthquake and Volcano Deformation*, Princeton Univ. Press, pp. 1–457.

Thomas, M.Y., Avouac, J.-P., Champenois, J., Lee, J.-C. & Kuo, L.-C., 2014. Spatiotemporal evolution of seismic and aseismic slip on the Longitudinal Valley Fault, Taiwan. *J. geophys. Res.,* **119,** 5114–5139.

Thompson, T. B., Plesch, A., Shaw, J. H. & Meade, B. J., 2015. Rapid slip-deficit rates at the eastern margin of the Tibetan Plateau prior to the 2008 Mw 7.9 Wenchuan earthquake, *Geophys. Res. Lett.,* **42,** 1677–1684.

Tibaldi, A., Rovida, A. & Corozzato, C., 2007. Late Quaternary kinematics, slip-rate and segmentation of a major Cordillera-Parallel transcurrent fault: the Cayambe-Afiladores-Sibundoy system, NW south America, *J. Struct. Geol.,* **29**(4), 664–680.

Vaca, S., Vallée, M., Nocquet, J. M. & Alvarado, A., 2019. Active deformation in Ecuador enlightened by a new waveform-based catalog of earthquake focal mechanisms. *J. S. Am. Earth Sci.,* **93,** 449–461.

Williams, S., 2005. Create and Analyse Time Series: CATS software V3.1.1, 1–13.

Yepes, H., Audin, L., Alvarado, A., Beauval, C., Aguilar, J., Font, Y. & Cotton, F., 2016. A new view for the geodynamics of Ecuador: implication in seismogenic source definition and seismic hazard assessment, *Tectonics,* **35,** 1249–1279.

SUPPORTING INFORMATION

Supplementary data are available at *GJI* online.

Figure S1: Results for a selection of models and fit to GPS and InSAR data. Column 1: Slip distribution. Slip values are indicated by the colour scale on the right-hand side of the subplots on mm yr^{-1}. Horizontal shortening rate (mm yr^{-1}), depth (km) and dip (°) and

indicated above each subplot. Column 2: Arrows indicate observations (blue), models (red) and residuals (black), respectively. The wrms of residuals is labelled on top of each subplot. Column 3: LOS rate model predictions (mm yr^{-1}). Column 4: LOS rate observations (mm yr^{-1}). Column 5: LOS rate residuals (mm yr^{-1}). All LOS rate maps use the same colour code indicated on the right-hand side of the figure. The selected best models from Fig. 8 are the last four, with a fault dipping at 20° west and with a shortening rate between 4.6 and 4.9 mm yr^{-1}.

Figure S2: Same as Fig. S1 with slip $= V_h$. The long-term slip rate on the ramp is equal to the shortening rate V_h.

Figure S3: Distribution of the seismicity in the Quito area issued from the IG-EPN Catalogue (2011–2016). Earthquakes are selected starting from MLv 2 + and until 40 km deep, with an error in the depth location of less than 5 km. Top left is the histogram representing the number of earthquakes versus depth, with more than 80 per cent of the seismicity located above 10 km depth.

Figure S4: Quito Fault recurrence models based either on seismicity (red line) or on total geodetic moment rates (black dashed lines), with a *b*-value = 0.81 (Beauval *et al.* 2014). (a) Maximum magnitude based on scaling laws (Leonard 2010) with $M_{max} = 7.3$; (b) $M_{max} = 6.8$ to obtain the same annual exceedance rate for the G-R based on the minimal moment rate ($0.3x10^{17}$ N m yr^{-1}) and the G-R based on the seismicity.

Figure S5: East component times-series of GPS sites used in this study. The raw time-series are expressed in the stable foot wall reference frame as described in Section 4.2. The dotted line shows the estimated velocity.